Double Dirac nodal lines enforced by multiple nonsymmorphic symmetries

Gijeong An ®,[1,*] Yoonseok Hwang ®,[2,3,4,5,*] Yunjae Kim,[6,*] Changmo Kang ®,[1] Yoonah Chung ®,[1] Minsu Kim,[1] Seyeong Cha,[1] Changmin Jin,[1] Yeryn Kim,[1] Suklyun Hong ®,[6,†] Bohm-Jung Yang ®,[2,3,4,5,‡] and Keun Su Kim ®[1,§]

[1]*Department of Physics, Yonsei University, Seoul 03722, Republic of Korea*
[2]*Department of Physics and Astronomy, Seoul National University, Seoul 08826, Republic of Korea*
[3]*Center for Correlated Electron Systems, Institute for Basic Science (IBS), Seoul 08826, Republic of Korea*
[4]*Center for Theoretical Physics (CTP), Seoul National University, Seoul 08826, Republic of Korea*
[5]*Institute of Applied Physics, Seoul National University, Seoul 08826, Republic of Korea*
[6]*Department of Physics, Graphene Research Institute, and GRI-TPC International Research Center,*
Sejong University, Seoul 05006, Republic of Korea

The topological quantum states of matter can be characterized by the geometric form and number of symmetry-enforced band degeneracy, such as nodal points, lines, and surfaces from twofold up to eightfold degeneracy. Here, we report the observation of double Dirac (fourfold) nodal lines stabilized by multiple nonsymmorphic symmetries in puckered honeycomb systems, black phosphorus, and metal monochalcogenides. By angle-resolved photoemission spectroscopy, we found a fourfold (Dirac) nodal line running along the armchair zone boundary of black phosphorus, reproduced by first-principles band calculations and proven by our symmetry analysis to be protected by space-time inversion and glide-mirror symmetries. The presence of the multiple glide-mirror symmetries in its binary counterpart, GeS, diversifies into five Dirac nodal lines, two of which come closer at the zigzag zone boundary to form a nearly eightfold nodal line. Our results demonstrate the correspondence between nonsymmorphicity and band degeneracy with puckered honeycomb systems.

I. INTRODUCTION

In the band theory of solids, materials can be classified into the metals and the insulators. This conventional classification was recently diversified based on the concept of topological phases in electronic structures [1,2]. In this framework, the materials can be classified into the topologically trivial one and the topologically nontrivial one, the latter of which includes topological insulators [3–6], topological semimetals [7–12], and superconductors [13]. Indeed, this class of materials has served as a platform to study various topological quantum states, such as quantum spin Hall states [3–5], Dirac or Weyl semimetal states [11,12], quantum anomalous Hall states [14,15], Majorana bound states [16], and so forth.

The class of topological materials can be characterized by the geometric form and number of symmetry-enforced band degeneracy in k space. A well-known example of two-dimensional (2D) Dirac semimetals is graphene, in which spin-degenerate conduction and valence bands meet each other at the K points, constituting the Dirac point with nearly fourfold degeneracy [3]. This Dirac node can be part of the higher-dimensional objects, such as 1D nodal lines [17–19] or loops [20] and 2D nodal surfaces [21] protected by the combination of crystal symmetries including glide-mirror and screw-rotation symmetries. The presence of

such nonsymmorphic symmetries renders the number of band degeneracy at nodes as one of threefold [22,23], fourfold (Dirac) [10,11], sixfold [24], and eightfold [25]. This eightfold is the maximum possible number of band degeneracy allowed by space-group symmetries in real materials as a 3D spinful system [26].

In this respect, it is fundamentally important to understand the correspondence between nonsymmorphicity and band degeneracy. However, it has been extremely challenging to experimentally address this issue owing to the lack of simple (toy model) systems having a systematic variation in nonsymmorphic symmetries. A potential candidate that can be used for that purpose is the family of materials with puckered honeycomb structures, such as black phosphorus (BP) and group-IV metal monochalcogenides (MX, $M =$ Ge and Sn, $X =$ S and Se). The crystal structure of BP has the honeycomb network of A and B sublattices as in graphene, but it is modulated up and down to be armchair-shaped along x, as shown in Figs. 1(a) and 1(b). This forms alternative upper and lower zigzag chains running along y, resulting in glide-mirror symmetry in x with the half translation in y, which is denoted as $\tilde{M}_x$ [light red line in Fig. 1(a)]. Indeed, the presence of $\tilde{M}_x$ was invoked to explain the pair of Dirac points observed in the band-inverted regime of BP [27,28].

On the other hand, MX has the same puckered honeycomb structure as BP. As compared in Figs. 1(a) and 1(c), however, a key difference is that there are two different elements in the A and B sublattice of the upper and lower zigzag chains in MX. That is, the relation of BP and MX is interestingly similar to that of graphene and hexagonal boron

*These authors contributed equally to this work.
†hong@sejong.ac.kr
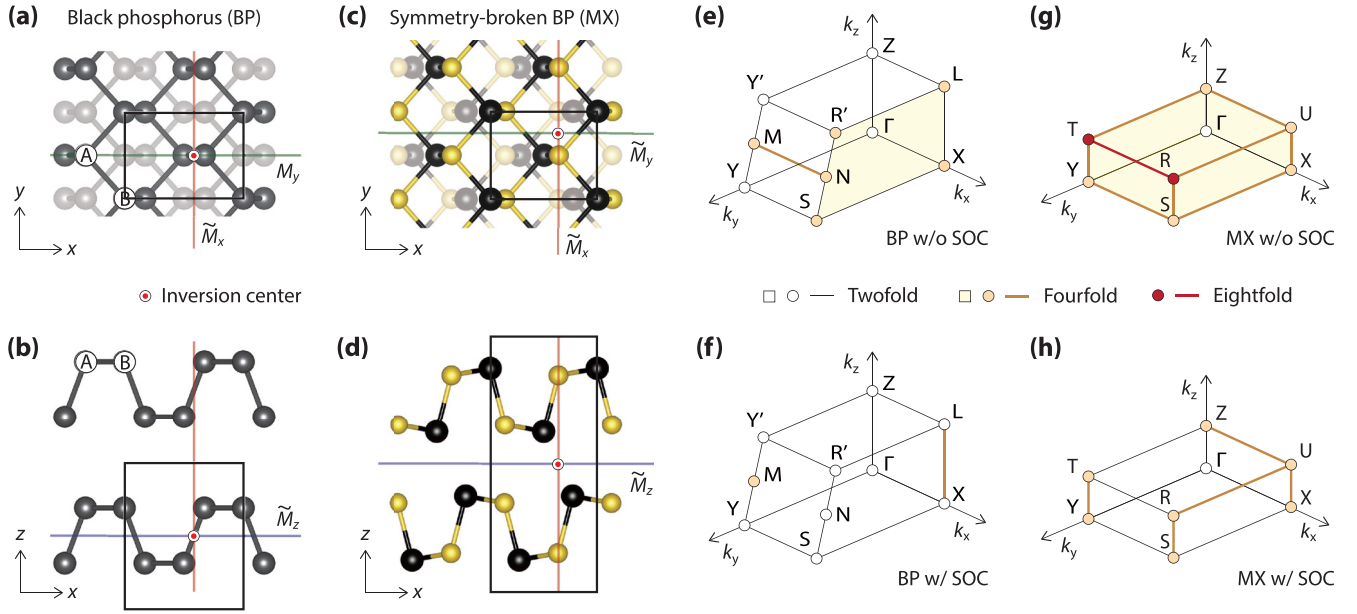‡bjyang@snu.ac.kr
§keunsukim@yonsei.ac.kr

FIG. 1. Ball-and-stick model of BP [panels (a) and (b)] and *MX* [panels (c) and (d)], viewed from the top [panels (a) and (c)] and side [panels (b) and (d)]. Gray, black, and yellow balls represent P, *M* (Ge or Sn), and *X* (S or Se) atoms, respectively. The black rectangles show the primitive unit cell. The light red, green, and blue lines are the plane of mirror (or glide-mirror) symmetries in *x*, *y*, and *z*, respectively, with respect to the inversion center marked by the circled red dot. The two sublattices of BP in a sublayer are marked by the circled A and B. (e)–(h) Brillouin zone of BP [panels (e) and (f)] and *MX* [panels (g) and (h)] plotted for $k_x > 0$, $k_y > 0$, and $k_z > 0$ (octant). The band degeneracy of BP and MX is obtained by our symmetry analysis without considering spin-orbit coupling (w/o SOC) [panels (e) and (g)] and with spin-orbit coupling (w/ SOC) [panels (f) and (h)]. As for w/o SOC in panels (e) and (g), the spin up and spin down are doubly counted. The number of band degeneracy at vertices, edges, and faces of the Brillouin zone is indicated by markers defined at the bottom of panels (e) and (g).

nitrides (h-BN). In the sense that h-BN can be viewed as graphene with broken A-B sublattice symmetry, *MX* can also be described as a symmetry-broken analog of BP [29]. This broken sublattice symmetry renders *MX* to have the unit cells doubled in the *z* direction as compared to those of BP [black boxes in Figs. 1(b) and 1(d)], thereby making it with more nonsymmorphic symmetry elements. Therefore, this family of puckered honeycomb crystals is a great platform to systematically trace how variations in nonsymmorphic symmetries affect the geometric form and number of band degeneracy. Here, we have studied symmetry-enforced band degeneracy in BP and *MX* by angle-resolved photoemission spectroscopy (ARPES), density-functional-theory (DFT) calculations, and symmetry analysis.

II. ARPES EXPERIMENTS AND BAND CALCULATIONS

We have conducted ARPES experiments at Beamline 7.0.2 (MAESTRO), the Advanced Light Source. The microARPES endstation is equipped with the hemispherical spectrometer with energy and angular resolutions better than 20 meV and 0.1°, respectively. The monochromatized synchrotron radiation with the incident angle of 54.75° from normal to samples was focused to approximately 30 μm in diameter on the surface of samples. ARPES data were taken at the sample temperature of 15–30 K, down to which any signature of charging is observed. Single crystals of BP and GeS with a purity better than >99.995% were grown by the high-pressure technique and chemical vapor transport, respectively (HQ graphene). The grown samples were characterized by

x-ray diffraction, Raman spectroscopy, and energy-dispersive x-ray spectroscopy. Each piece of sample was glued on the copper sample holder using conductive silver epoxy. The clean surface of BP and GeS was prepared *in situ* by cleaving in the ultrahigh vacuum chamber with the base pressure better than 4×10^{-11} torr. The Fermi level was calibrated by taking reference spectra from copper sample holders and by depositing alkali metals to metallize the surface of samples.

The theoretical band structures of GeS and BP were calculated based on DFT using the generalized gradient approximation for the exchange-correlation functionals, implemented in the Vienna *ab initio* simulation package (VASP) [30]. The kinetic energy cutoff was set to 300 eV, and electron-ion interactions were represented by projector-augmented wave potentials [31]. The lattice constants of bulk GeS were calculated as $a = 4.30$ Å, $b = 3.64$ Å, and $c = 10.47$ Å, while those of bulk BP were calculated as $a = 4.43$ Å, $b = 3.31$ Å, and $c = 5.68$ Å, with $\alpha = 106.6°$ and $\beta = \gamma = 90°$. We used a $(10 \times 12 \times 4)$ *k*-point grid for bulk GeS and a $(10 \times 12 \times 8)$ *k*-point grid for bulk BP in the Γ-centered *k*-point scheme for atomic optimizations and the Brillouin zone integration. Hellmann-Feynman forces were kept to less than 0.01 eV/Å for ionic relaxation.

III. NODAL STRUCTURE OF BP

The crystal structure of bulk BP (space group 64, *Cmce*) is shown in Figs. 1(a) and 1(b), where there are four basis P atoms in the primitive cell. This orthorhombic structure has
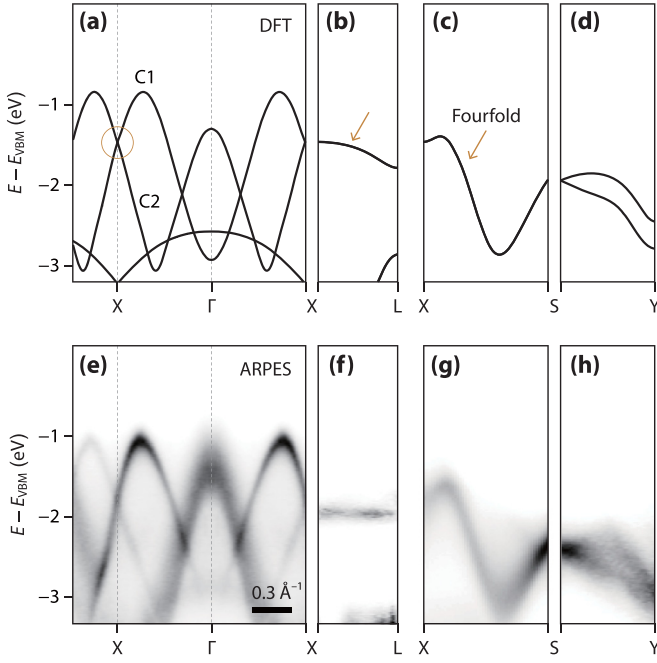
FIG. 2. (a)–(d) Theoretical electronic structure of bulk BP, calculated by DFT in the absence of spin-orbit coupling (w/o SOC) and shown in high-symmetry directions introduced in Fig. 1(e). The orange circle in panel (a) marks the crossing of C1 and C2 bands, and orange arrows in panels (b) and (c) indicate fourfold (Dirac) degenerate nodal lines. (e)–(h) Experimental electronic structure of BP, taken by ARPES and shown in high-symmetry directions corresponding to those in panels (a)–(d). Data shown in panel (e) are symmetrized with respect to the Γ point. Experimental conditions in the order of photon energy, polarization, and scattering plane are as follows: (e) 145 eV, p-pol, yz; (f) 63–83 eV, p-pol, yz; (g) 145 eV, p-pol, yz; and (h) 145 eV, s-pol, yz. The sample temperature was kept at 16 ± 4 K during measurements.

the four major symmetry elements: time reversal T, inversion P, $\tilde{M}_x$, and mirror in y (M_y) shown by the light green line in Fig. 1(a). Figure 1(e) shows the Brillouin zone for $k_x > 0$, $k_y > 0$, and $k_z > 0$ (octant) with the major high-symmetry points. Because the spin-orbit coupling of BP and MX is typically weak [27], it is more comprehensible to first introduce their band structure on the assumption that spin up and spin down are degenerated, namely, without spin-orbit coupling (w/o SOC), and then to explain how it changes with spin-orbit coupling (w/ SOC). For the degeneracy w/o SOC, both spin-up and spin-down bands are counted.

Figure 2 compares the theoretical band structure of bulk BP obtained by DFT calculations and the experimental one obtained by ARPES. As expected from DFT calculations in the X-Γ-X direction [Fig. 2(a)], we found two dispersive bands labeled C1 and C2 [Fig. 2(e)]. They have lower binding energies near X rather than Γ, because the valence band maximum of BP is located at Z [32]. The spectral width of those near X appears narrower than that of those near Γ, because their orbital character near X is mainly p_x with little dispersion along k_z, whereas that near Γ is p_z. The spectral intensity of C1 and C2 is asymmetric due to their pseudospin characters [33], which is interestingly reversed across X. Related to that,

C1 and C2 bands seem to cross each other at the X point, as marked by the orange circle. This fourfold degeneracy of C1 and C2 (w/o SOC) at the X point is kept along X-L [Figs. 2(b) and 2(f)] and along X-S [Figs. 2(c) and 2(g)]. It is, however, lifted off the $k_x = \pi$ plane, as in S-Y [Figs. 2(d) and 2(h)]. A small discrepancy that can be noticed in X-L is that k_z dispersion is flatter in ARPES [Fig. 2(f)] than in DFT [Fig. 2(b)], which may come from surface states or stacking disorder.

The fourfold degeneracy of BP can be proven by our symmetry analysis without considering spin-orbit coupling. The number of band degeneracy, which is enforced by symmetries, and so regardless of models or system details, is summarized in Fig. 1(e) (for the fuller description, see Supplemental Material [34]). We found that there exists the fourfold (Dirac) nodal surface at the armchair zone boundary or that enclosed by R′ LXS lines [light yellow region in Fig. 1(e)], which naturally explains our experimental findings in Figs. 2(e)–2(g). From this symmetry analysis [34], this fourfold nodal surface at $k_x = \pi$ (w/o SOC) is protected by $\tilde{M}_x$ and space-time inversion symmetry defined by $I_{ST} = PT$. Although not the focus of this study, there is another fourfold nodal line at M-N, which is protected by I_{ST} and twofold screw-rotation symmetry $\tilde{C}_{2x} = P\tilde{M}_x$.

IV. NODAL STRUCTURE OF MX

As demonstrated with BP thus far, the presence of I_{ST} and $\tilde{M}_x$ leads to the fourfold nodal surface at $k_x = \pi$ (w/o SOC). In this sense, it would be interesting to see how it changes with the binary counterpart of BP, which is MX. The bulk form of MX (space group 62, $Pnma$) has basically the same puckered honeycomb structure as in BP, but the two sublattices in each sublayer consist of different elements [Figs. 1(c) and 1(d)]. It renders the unit cell of MX doubled in the z direction (black boxes), leading to multiple glide-mirror symmetries ($\tilde{M}_x$, $\tilde{M}_y$, and $\tilde{M}_z$) shown by light red, green, and blue lines, respectively. Figure 1(g) shows the Brillouin zone of MX with the number of band degeneracy taken from symmetry analysis (w/o SOC). Indeed, there is the fourfold (Dirac) nodal surface at each $k_i = \pi$, where $i = x$, y, and z [light yellow areas in Fig. 1(g)], which is found protected by I_{ST} and $\tilde{M}_i$, respectively [34].

The presence of fourfold nodal surfaces at $k_i = \pi$ in real MX materials can be demonstrated by both first-principles band calculations and experiments. We chose GeS as a prototype of MX materials, but the following discussions can also be applied to the other MX's. In Fig. 3, we compare the theoretical band structure of GeS obtained by DFT to the experimental one taken by ARPES. As expected from DFT band calculations in Fig. 3(a), there are four dispersive bands labeled C3–C6 in the X-Γ-X direction [Fig. 3(e)]. It can be clearly identified at the X point that the pair of C3 and C4 bands and the pair of C5 and C6 bands cross each other, as indicated by orange circles. More importantly, this fourfold degeneracy of each band pair is retained along the X-U-R-S line [Figs. 3(b) and 3(f)], enclosing the $k_x = \pi$ plane [for X-U in Fig. 3(f), the band at –0.2 eV looks sharper than that at –1 eV due to their difference in k_z dispersion]. Likewise,
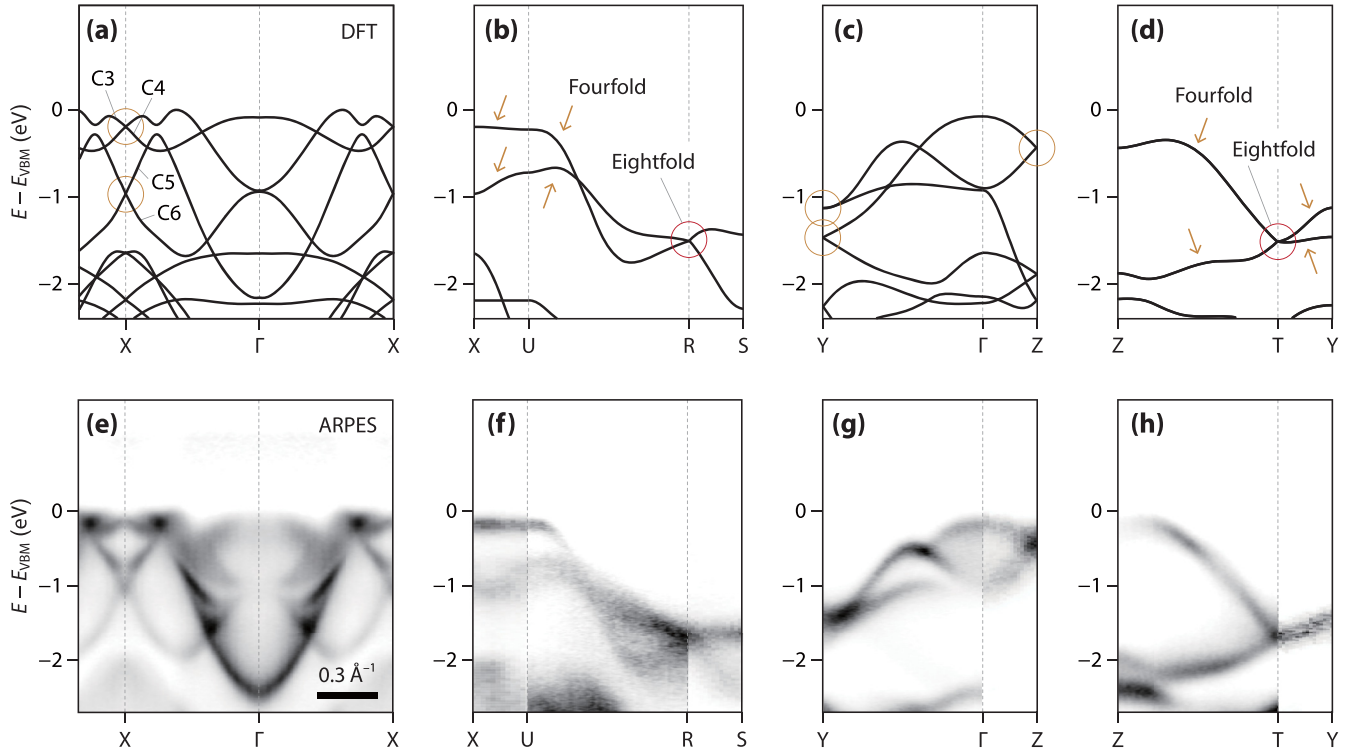
FIG. 3. (a)–(d) Theoretical electronic structure of bulk GeS, calculated by DFT in the absence of spin-orbit coupling (w/o SOC) and shown in high-symmetry directions introduced in Fig. 1(g). Orange and red circles indicate fourfold and nearly eightfold degenerate nodes, respectively, and the orange arrows indicate fourfold nodal lines. (e)–(h) Experimental band structure of GeS taken by ARPES and shown in high-symmetry directions corresponding to those in panels (a)–(d). Data shown in panel (e) are symmetrized with respect to the Γ and X points. Experimental conditions in the order of photon energy, polarization, and scattering plane are as follows: (e) 106 eV, *s*-pol, *yz*; (f) 129–141 eV, *s*-pol, *yz* for XU, 124 eV, *p*-pol, *yz* for UR, 198–213 eV, *p*-pol, *sz* for RS; (g) 200–213 eV, *p*-pol, *yz* for ΓZ; and (h) 119 eV, *s*-pol, *yz* for ZT, 97–108 eV, *s*-pol, *xz* for TY. The sample temperature was kept at 25 ± 4 K during measurements.

we found similar fourfold nodal surfaces at both $k_y = \pi$ and $k_z = \pi$ [orange circles in Figs. 3(c) and 3(g)].

Another remarkable point in the ARPES data of bulk GeS is that the two fourfold nodal lines in U-R-S [Figs. 3(b) and 3(f)] seem to meet each other at the R point marked by the red circle, leading to eightfold degeneracy (w/o SOC). Furthermore, this eightfold degeneracy at the R point is retained along the T-R line [red line in Fig. 1(g)], as demonstrated by ARPES data taken along Z-T-Y [Figs. 3(d) and 3(h)]. Note that one of two bands in T-Y at a higher binding energy is not observed due to the matrix element effect. It is important to check the stability of this eightfold nodal line at T-R and fourfold nodal surfaces at $k_i = \pi$ ($i = x, y,$ and z) against spin-orbit coupling. Although the strength of spin-orbit coupling in BP and GeS is comparable to the ARPES resolution, it is still possible by theoretical means (DFT) to see which of the observed nodal lines and surfaces is stable even in the presence of spin-orbit coupling.

V. EFFECT OF SPIN-ORBIT COUPLING

In Fig. 4(a), we show the DFT band structure (w/ SOC) of BP (black) and *MX* (yellow), which are simultaneously plotted with respect to the crossing energy. Since there is no spin-orbit gap at the crossing energy, the crossing of C1 and C2 bands at the X point of BP corresponds to the fourfold degenerate (Dirac) point. As shown in Fig. 4(b), this fourfold

degeneracy of BP is retained along X-L, constituting the Dirac nodal line (DNL). On the other hand, the fourfold nodal line observed in X-S [Fig. 2(g)] shows a minute splitting of about 2 meV by the effect of spin-orbit coupling [Fig. 4(b)]. That is, fourfold degeneracy in the nodal surface at $k_x = \pi$ [Fig. 1(e)] is lifted but the X-L line, as summarized in Fig. 1(f). Our symmetry analysis [34] proves that the DNL of BP at X-L running along the z direction is protected by I_{ST}, $\tilde{M}_x$, and M_y even in the presence of spin-orbit coupling.

If this relation of nonsymmorphic symmetries to band degeneracy is universal, the presence of multiple glide-mirror symmetries in *MX* is expected to stabilize more DNLs. In Fig. 4(a), we show the calculated band structure of GeS for the crossing of C3 and C4 bands and that of C5 and C6 bands at the X point. Since there is no spin-orbit gap at the crossing energy, those at the X point [Figs. 3(a) and 3(e)] correspond to the Dirac points. As shown in Fig. 4(c), this fourfold degeneracy is maintained along X-U, U-R, and T-Y, showing the existence of multiple DNLs. That is, fourfold degeneracy in the nodal surface of *MX* at $k_i = \pi$ [Fig. 1(g)] is lifted but the five DNLs in Z-U, U-R, X-U, S-R, and Y-T, as summarized in Fig. 1(h). From our symmetry analysis [34], we prove that the former four DNLs running along the i direction are protected by I_{ST}, $\tilde{M}_j$, and $\tilde{M}_k$, where $i, j, k = x, y, z$ and $i \neq j \neq k$.

As for the eightfold degeneracy of GeS at T-R (w/o SOC), the effect of spin-orbit coupling opens a small gap, resulting in minutely split four bands of twofold degeneracy, as shown
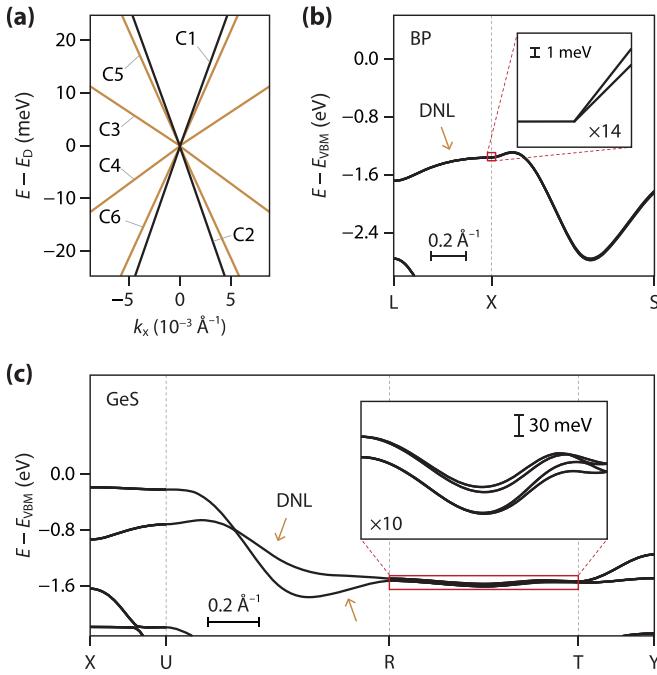
FIG. 4. (a) Band structure of BP (black) and GeS (yellow) obtained by DFT in the presence of spin-orbit coupling (w/ SOC). The C1 and C2 bands of BP in Fig. 2(a) and C3– C6 bands of GeS in Fig. 3(a) are simultaneously plotted with respect to the Dirac energy (E_D) and X points. (b) Band structure of BP obtained by DFT (w/ SOC) and plotted along L-X-S. The inset in panel (b) is the magnified view of the band structure indicated by the red box. (c) Band structure of GeS obtained by DFT (w/ SOC) and plotted along X-U-R-T-Y. The inset in panel (c) shows the magnified view of the band structures indicated by the red box. The orange arrows in panels (b) and (c) show DNLs.

in inset of Fig. 4(c). This spin-orbit gap is estimated by DFT calculations to be 20 ± 9 meV with its minimum at the T point (11 meV) and its maximum at the R point (29 meV). The symmetry origin of this nearly eightfold degenerate nodal line at T-R should thus be traced back to the eightfold degeneracy of GeS at T-R in the absence of spin-orbit coupling [Fig. 1(g)], which is found protected by I_{ST}, $\tilde{M}_y$, and $\tilde{M}_z$ [34].

Finally, we would add remarks on another interesting object of symmetry-protected band degeneracy, which is the so-called hourglass nodal line [35]. If spin-orbit coupling is not considered (w/o SOC), there are hourglass nodal lines

of fourfold degeneracy in BP and MX at $k_x = 0$ (see Supplemental Material, Figs. S2, S4, and S5). As described in the Supplemental Material [34], these fourfold degenerate hourglass nodal lines are protected by $\tilde{M}_x$, which is a common symmetry element of BP and MX. Although it was not the focus of this study, it would be interesting to observe hourglass nodal lines in this family of puckered honeycomb materials with weak spin-orbit coupling in the forthcoming works.

VI. SUMMARY

In summary, we have investigated symmetry-enforced band degeneracy in the puckered honeycomb systems (BP and MX) by the combination of ARPES, DFT, and symmetry analysis. It was experimentally demonstrated and theoretically proven for a system with I_{ST} symmetry and weak spin-orbit coupling that (i) the presence of glide-mirror symmetry ($\tilde{M}_i$) stabilizes nearly fourfold degenerate nodal surfaces at $k_i = \pi$ and that (ii) the combination of two glide-mirror symmetries or a screw rotation symmetry ($\tilde{C}_{2i} = \tilde{M}_j \tilde{M}_k$) stabilizes the DNL(s) running along the i direction. We also found the double Dirac nodal lines of GeS in the x direction, which is proven enforced by I_{ST}, $\tilde{M}_y$, and $\tilde{M}_z$. Our results demonstrate the correspondence between nonsymmorphicity and band degeneracy with puckered honeycomb systems.

[1] C. K. Chiu, J. C. Y. Teo, A. P. Schnyder, and S. Ryu, Rev. Mod. Phys. **88**, 035005 (2016).

[2] M. Z. Hasan, G. Chang, I. Belopolski, G. Bian, S. Y. Xu, and J. X. Yin, Nat. Rev. Mater. **6**, 784 (2021).

[3] C. L. Kane and E. J. Mele, Phys. Rev. Lett. **95**, 226801 (2005).

[4] B. A. Bernevig, T. L. Hughes, and S. C. Zhang, Science **314**, 1757 (2006).

[5] D. Hsieh, D. Qian, L. Wray, Y. Xia, Y. S. Hor, R. J. Cava, and M. Z. Hasan, Nature (London) **452**, 970 (2008).

[6] M. Z. Hasan and C. L. Kane, Rev. Mod. Phys. **82**, 3045 (2010).

[7] S. M. Young, S. Zaheer, J. C. Y. Teo, C. L. Kane, E. J. Mele, and A. M. Rappe, Phys. Rev. Lett. **108**, 140405 (2012).

[8] B. J. Yang and N. Nagaosa, Nat. Commun. **5**, 4898 (2014).

[9] S. M. Young and C. L. Kane, Phys. Rev. Lett. **115**, 126803 (2015).

[10] Z. K. Liu, B. Zhou, Y. Zhang, Z. J. Wang, H. M. Weng, D. Prabhakaran, S. K. Mo, Z. X. Shen, Z. Fang, X. Dai, Z. Hussain, and Y. L. Chen, Science **343**, 864 (2014).

[11] Z. K. Liu, J. Jiang, B. Zhou, Z. J. Wang, Y. Zhang, H. M. Weng, D. Prabhakaran, S. K. Mo, H. Peng, P. Dudin, T. Kim, M.

Hoesch, Z. Fang, X. Dai, Z. X. Shen, D. L. Feng, Z. Hussain, and Y. L. Chen, Nat. Mater. **13**, 677 (2014).

[12] S. Y. Xu, I. Belopolski, N. Alidoust, M. Neupane, G. Bian, C. Zhang, R. Sankar, G. Chang, Z. Yuan, C.-C. Lee, S. M. Huang, H. Zheng, J. Ma, D. S. Sanchez, B. Wang, A. Bansil, F. Chou, P. P. Shibayev, H. Lin, S. Jia *et al.*, Science **349**, 613 (2015).

[13] X. L. Qi and S. C. Zhang, Rev. Mod. Phys. **83**, 1057 (2011).

[14] C. Z. Chang, J. Zhang, X. Feng, J. Shen, Z. Zhang, M. Guo, K. Li, Y. Ou, P. Wei, L. L. Wang, Z. Q. Ji, Y. Feng, S. Ji, Xi Chen, J. Jia, X. Dai, Z. Fang, S. C. Zhang, K. He, Y. Wang *et al.*, Science **340**, 167 (2013).

[15] R. Yu, W. Zhang, H. J. Zhang, S. C. Zhang, X. Dai, and Z. Fang, Science **329**, 61 (2010).

[16] K. Flensberg, F. von Oppen, and A. Stern, Nat. Rev. Mater. **6**, 944 (2021).

[17] C. Fang, Y. Chen, H.-Y. Kee, and L. Fu, Phys. Rev. B **92**, 081201(R) (2015).

[18] B.-J. Yang, T. A. Bojesen, T. Morimoto, and A. Furusaki, Phys. Rev. B **95**, 075135 (2017).

[19] L. M. Schoop, M. N. Ali, C. Strasser, A. Topp, A. Varykhalov, D. Marchenko, V. Duppel, S. S. P. Parkin, B. V. Lotsch, and C. R. Ast, Nat. Commun. **7**, 11696 (2016).

[20] M. Ezawa, Phys. Rev. Lett. **116**, 127202 (2016).

[21] W. Wu, Y. Liu, S. Li, C. Zhong, Z. M. Yu, X. L. Sheng, Y. X. Zhao, and S. A. Yang, Phys. Rev. B **97**, 115125 (2018).

[22] B. Q. Lv, Z. L. Feng, Q. N. Xu, X. Gao, J. Z. Ma, L. Y. Kong, P. Richard, Y. B. Huang, V. N. Strocov, C. Fang, H.-M. Weng, Y.-G. Shi, T. Qian, and H. Ding, Nature (London) **546**, 627 (2017).

[23] J. Z. Ma, J. B. He, Y. F. Xu, B. Q. Lv, D. Chen, W. L. Zhu, S. Zhang, L. Y. Kong, X. Gao, L. Y. Rong, Y.-B. Huang, P. Richard, C. Y. Xi, E. S. Choi, Y. Shao, Y. L. Wang, H. J. Gao, X. Dai, C. Fang, H. M. Weng *et al.*, Nat. Phys. **14**, 349 (2018).

[24] N. Kumar, M. Yao, J. Nayak, M. G. Vergniory, J. Bannies, Z. Wang, N. B. M. Schröter, V. N. Strocov, L. Müchler, W. Shi, E. D. L. Rienks, J. L. Mañes, C. Shekhar, S. S. P. Parkin, J. Fink, G. H. Fecher, Y. Sun, B. A. Bernevig, and C. Felser, Adv. Mater. **32**, 1906046 (2020).

[25] B. J. Wieder, Y. Kim, A. M. Rappe, and C. L. Kane, Phys. Rev. Lett. **116**, 186402 (2016).

[26] B. Bradlyn, J. Cano, Z. Wang, M. G. Vergniory, C. Felser, R. J. Cava, and B. A. Bernevig, Science **353**, aaf5037 (2016).

[27] J. Kim, S. S. Baik, S. H. Ryu, Y. Sohn, S. Park, B.-G. Park, J. Denlinger, Y. Yi, H. J. Choi, and K. S. Kim, Science **349**, 723 (2015).

[28] J. Kim, S. S. Baik, S. W. Jung, Y. Sohn, S. H. Ryu, H. J. Choi, B.-J. Yang, and K. S. Kim, Phys. Rev. Lett. **119**, 226801 (2017).

[29] F. Xia, H. Wang, J. C. M. Hwang, A. H. C. Neto, and L. Yang, Nat. Rev. Phys. **1**, 306 (2019).

[30] G. Kresse and J. Furthmüller, Phys. Rev. B **54**, 11169 (1996).

[31] G. Kresse and D. Joubert, Phys. Rev. B **59**, 1758 (1999).

[32] C. Q. Han, M. Y. Yao, X. X. Bai, L. Miao, F. Zhu, D. D. Guan, S. Wang, C. L. Gao, C. Liu, D. Qian, Y. Liu, and J.-F. Jia, Phys. Rev. B **90**, 085101 (2014).

[33] S. W. Jung, S. H. Ryu, W. J. Shin, Y. Sohn, M. Huh, R. J. Koch, C. Jozwiak, E. Rotenberg, A. Bostwick, and K. S. Kim, Nat. Mater. **19**, 277 (2020).

[34] See Supplemental Material at http://link.aps.org/supplemental/ 10.1103/PhysRevB.109.155146 for symmetry analysis on the nodal structure of BP and MX.

[35] R. Takahashi, M. Hirayama, and S. Murakami, Phys. Rev. B **96**, 155206 (2017).